APL Photonics

An optical coherence photoacoustic microscopy system using a fiber optic sensor

Cite as: APL Photonics **6**, 096103 (2021); https://doi.org/10.1063/5.0059351
Submitted: 08 June 2021 . Accepted: 12 August 2021 . Published Online: 03 September 2021

Shiyu Deng, Richard Haindl, Edward Zhang, Paul Beard, Eva Scheuringer, Caterina Sturtzel, Qian Li, Abigail J. Deloria, Harald Sattmann, Rainer A. Leitgeb, Yi Yuan, Leopold Schmetterer, Manojit Pramanik, Martin Distel, Wolfgang Drexler, Mengyang Liu, et al.

An optical coherence photoacoustic microscopy system using a fiber optic sensor

Cite as: APL Photon. 6, 096103 (2021); doi: 10.1063/5.0059351
Submitted: 8 June 2021 • Accepted: 12 August 2021 •
Published Online: 3 September 2021

Shiyu Deng,[1] Richard Haindl,[1] Edward Zhang,[2] Paul Beard,[2] Eva Scheuringer,[3] Caterina Sturtzel,[3] Qian Li,[1] Abigail J. Deloria,[1] Harald Sattmann,[1] Rainer A. Leitgeb,[1] Yi Yuan,[4] Leopold Schmetterer,[1,5,6,7,8,9,10] Manojit Pramanik,[7] Martin Distel,[3] Wolfgang Drexler,[1] and Mengyang Liu[1,a)]

AFFILIATIONS

[1] Center for Medical Physics and Biomedical Engineering, Medical University of Vienna, Währinger Gürtel 18-20, AKH 4L, 1090 Vienna, Austria
[2] Department of Medical Physics and Biomedical Engineering, University College London, Gower Street, WC1E 6BT London, United Kingdom and Wellcome/EPSRC Center for Interventional and Surgical Sciences, University College London, Gower Street, WC1E 6BT London, United Kingdom
[3] Innovative Cancer Models, St. Anna Children's Cancer Research Institute, Zimmermannplatz 10, 1090 Vienna, Austria
[4] Institute of Electrical Engineering, Yanshan University, 066004 Qinhuangdao, Hebei, China
[5] Department of Clinical Pharmacology, Medical University of Vienna, Währinger Gürtel 18-20, Floor 6, 1090 Vienna, Austria
[6] Singapore Eye Research Institute, The Academia Building, 20 College Road, Discovery Tower, Level 6, 169856 Singapore
[7] School of Chemical and Biomedical Engineering, Nanyang Technological University, 62 Nanyang Drive, 637459 Singapore
[8] SERI-NTU Advanced Ocular Engineering (STANCE) Laboratory, Singapore
[9] Ophthalmology and Visual Sciences Academic Clinical Program, Duke-NUS Medical School, 8 College Road, 169857 Singapore
[10] Institute of Molecular and Clinical Ophthalmology Basel, Mittlere Strasse 91, CH-4031 Basel, Switzerland

[a)] **Author to whom correspondence should be addressed:** mengyang.liu@meduniwien.ac.at

ABSTRACT

In this work, a novel fiber optic sensor based on Fabry–Pérot interferometry is adopted in an optical coherence photoacoustic microscopy (OC-PAM) system to enable high-resolution *in vivo* imaging. The complete OC-PAM system is characterized using the fiber optic sensor for photoacoustic measurement. After characterization, the performance of the system is evaluated by imaging zebrafish larvae *in vivo*. With a lateral resolution of 3.4 μm and an axial resolution of 3.7 μm in air, the optical coherence microscopy subsystem visualizes the anatomy of the zebrafish larvae. The photoacoustic microscopy subsystem reveals the vasculature of the zebrafish larvae with a lateral resolution of 1.9 μm and an axial resolution of 37.3 μm. As the two modalities share the same sample arm, we obtain inherently co-registered morphological and vascular images. This OC-PAM system provides comprehensive information on the anatomy and vasculature of the zebrafish larvae. Featuring compactness, broad detection bandwidth, and wide detection angle, the fiber optic sensor enables a large field of view with a static sensor position. We verified the feasibility of the fiber optic sensor for dual-modality *in vivo* imaging. The OC-PAM system, as a non-invasive imaging method, demonstrates its superiority in the investigation of zebrafish larvae, an animal model with increasing significance in developmental biology and disease research. This technique can also be applied for functional as well as longitudinal studies in the future.

I. INTRODUCTION

In the past couple of decades, optical coherence tomography (OCT)[1,2] and photoacoustic imaging (PAI)[3–5] have been developed and applied widely in biomedical and clinical research. Based on the interference of back-scattered light, OCT can reconstruct the sample in three-dimensions (3D) with high resolution and high speed. In addition, contrast-enhanced and functional OCT applications have also been demonstrated.[6,7] On the other hand, PAI, as a non-invasive modality that combines optical excitation and ultrasonic detection, can visualize endogenous chromophores and provide absorption information.[8] To combine the advantages of the two modalities, optical coherence photoacoustic microscopy (OC-PAM) systems have been explored and tested in various implementations.[9–13]

In terms of photoacoustic pulse detection, OC-PAM systems normally use piezoelectric transducers.[14–17] However, the field of view (FOV) of such transducers is limited by either the acoustic focal spot size or the transducer dimension. For higher sensitivity, the commonly used piezoelectric transducers usually have a large size and are opaque, which require a long working distance and make the system bulky. In contrast, remote sensing, which requires no coupling medium, is more feasible for preclinical and clinical applications and attracts considerable attention since its introduction.[8,18–20] In addition, the use of a single Michelson interferometer for both optical coherence microscopy (OCM) and photoacoustic microscopy (PAM) imaging has been demonstrated.[21,22] Nonetheless, due to the high sensitivity of the interferometer, unwanted environment interference could not be excluded from the measurements.[8] As an alternative, all-optical sensors based on a Fabry–Pérot interferometer (FPI) are developed for PAM imaging. An akinetic FPI sensor[23] has been successfully applied in an OC-PAM system and achieved high-resolution morphological and functional *in vivo* imaging even with a limited detection bandwidth.[9,24]

In this work, a novel fiber optic sensor, which was fabricated by depositing a miniaturized FPI on the tip of a single-mode fiber,[25] was adopted in a dual-modality OC-PAM system for *in vivo* imaging. Compared with other types of PAM detectors, the fiber optic sensor has advantages such as a small size, broad detection bandwidth, and almost omnidirectional detection. Therefore, it enables a simple system configuration and a large FOV with a stationary sensor.[26,27]

The performance of the system was evaluated by imaging the zebrafish (*Danio rerio*) larvae *in vivo*. Due to advantages such as external fertilization, fast embryonic development, small body size, and high optical transparency, zebrafish embryos are commonly used for studying the vasculature development in vertebrates. Furthermore, *Danio rerio* has recently become more prominent as an animal model for various diseases.[28–31]

In summary, in this work, we characterized an OC-PAM system using a novel fiber optic sensor and verified its feasibility for *in vivo* preclinical imaging. The results encourage further functional and longitudinal studies using the zebrafish and other small animal models.

II. METHODS AND RESULTS

A. The fiber optic sensor

The key component of the fiber optic sensor is a planoconcave micro-resonator, which is placed at the tip of a standard single-mode fiber [Fig. 1(a) inset]. To fabricate such a micro-resonator, a droplet of liquid UV-curable polymer is solidified on a highly reflective flat mirror. Due to the surface tension, the polymer droplet forms a dome shape. Another highly reflective mirror is then coated above the polymer to compose an etalon. Owing to the dome shape of the cavity, the walk-off of the laser beam within the micro-resonator is minimized, which contributes to a sharp sensor transfer function and a high sensitivity.[25]

To evaluate the performance of the fiber optic sensor, the frequency response, the noise-equivalent pressure (NEP), and the dynamic range of the sensor are characterized. An ultrathin layer of gold (AU.0100.ALSI, Platypus Technologies, LLC) was excited by the PAM system to measure the frequency response of the fiber optic sensor,[32] which is shown in Fig. 1(b). The fiber optic sensor has a non-uniform response of up to 50 MHz and has its maximum response at 14 MHz. NEP is one way to quantify the sensitivity of acoustic sensors and is defined as the acoustic pressure when the signal-to-noise ratio is unity.[26] The lower the NEP, the higher the sensitivity of the sensor. In this work, the NEP of the fiber optic sensor was measured using the procedure described in a previous study.[33] The NEP of this fiber optic sensor is compared with that of the akinetic sensor, which also uses all-optical detection of acoustic pulses.[9] Figure 1(c) shows the setup used for the NEP measurements. In brief, a 5 MHz piezoelectric transducer (V326, 5.0/.375, 201671, Panametrics) was driven by a signal generator to emit an acoustic burst (ten cycles per burst with a 10 kHz repetition rate). The fiber optic sensor and the akinetic sensor were positioned 30 cm away from the piezoelectric transducer to detect the signal in the far field region of this transducer. Both the emitter and the receiver were immersed in water to minimize acoustic attenuation. A calibrated hydrophone (SN2305, Precision Acoustics) was used as a reference for the NEP measurement. Figure 1(d) shows the normalized response of the fiber optic sensor and the akinetic sensor. Between 1 and 10 MHz acoustic frequency range, the fiber optic sensor has the maximum response at 6 MHz, whereas the akinetic sensor peaks at 1 MHz and is not able to detect signals above 4 MHz. In the 1–2 MHz frequency range, the waveforms measured by the fiber optic sensor were heavily distorted and had a low signal-to-noise ratio. Therefore, the response of the fiber optic sensor in this range is excluded in Fig. 1(d). Figures 1(e) and 1(f) display the waveforms detected by the akinetic sensor and the fiber optic sensor, respectively. To achieve higher accuracy in NEP calculation, the data in the red boxes of Figs. 1(e) and 1(f) were replaced by data measured with a higher amplitude resolution. Sine both sensors show non-uniform frequency responses, the NEPs were estimated at the maximum peak response frequencies. By calculating the root mean square noise before the arrival of the acoustic burst over a 20 MHz measurement bandwidth, the NEP of the akinetic sensor was quantified to be around 2.2 Pa at 1 MHz, and the NEP of the fiber optic sensor was around 42.2 Pa at 6 MHz. The dynamic range of the fiber optic sensor was measured to be around 55.5 dB according to Eq. (1), where P_{max} is the maximum undistorted pressure the fiber optic sensor can measure and P_{min} is the minimum detectable pressure,

$$\text{dynamic range} = 20 \times \log_{10}\left(\frac{P_{max}}{P_{min}}\right). \quad (1)$$

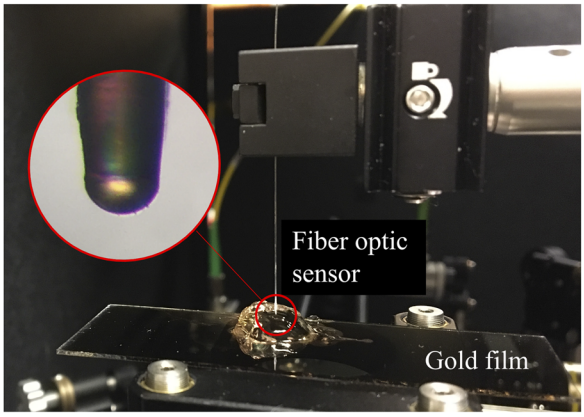

(a)

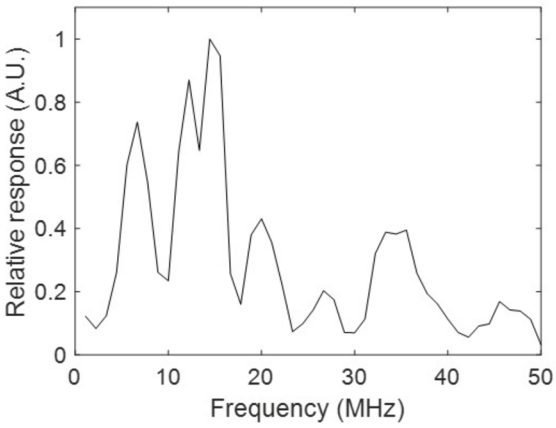

(b)

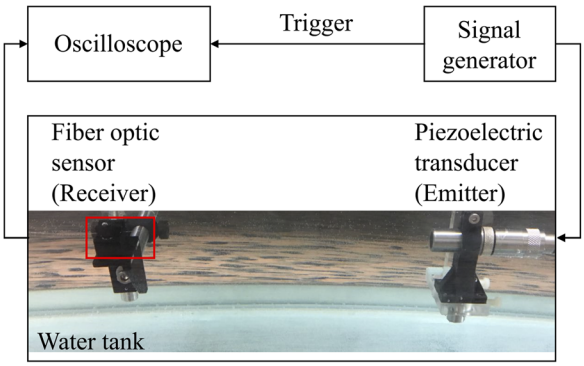

(c)

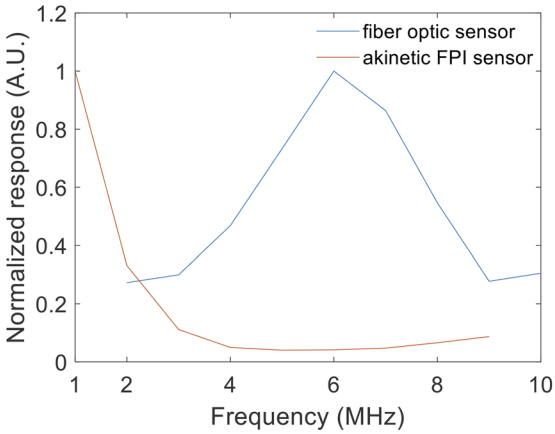

(d)

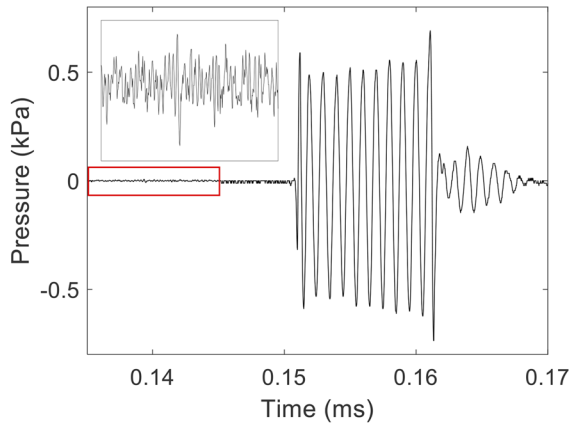

(e)

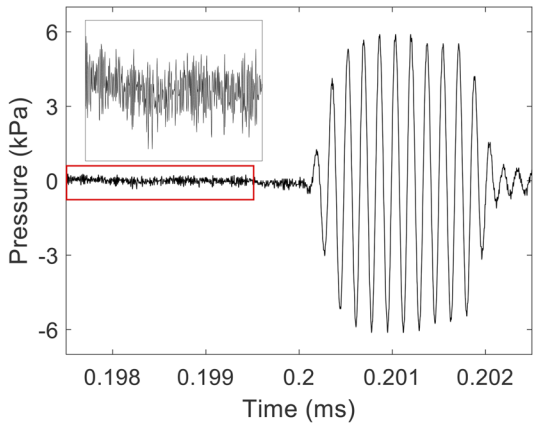

(f)

FIG. 1. Characterization experiments: (a) The setup for the frequency response measurement of the fiber optic sensor (inset: the brightfield microscopy image of the fiber optic sensor tip). (b) The normalized frequency response of the fiber optic sensor. (c) The schematic of the noise-equivalent pressure measurements. (d) The normalized frequency responses of the fiber optic sensor and the akinetic sensor in the range between 1 and 10 MHz (the response of the fiber optic sensor between 1 and 2 MHz is not shown due to the inaccuracy caused by the heavy distortion of the waveform and the low signal-to-noise ratio). (e) The pressure waveform detected by the akinetic sensor at 1 MHz acoustic frequency (inset: the zoomed in view of the noise in the red box region). (f) The pressure waveform detected by the fiber optic sensor at 6 MHz acoustic frequency (inset: the zoomed in view of the noise in the red box region).

B. The OC-PAM system

The schematic of the OC-PAM system is presented in Fig. 2(a). A flip mirror was used to toggle between the two imaging modalities, and the OCM and PAM images were acquired sequentially.

The OCM subsystem employed a compact prototype polarization-aligned three-superluminescent-diode laser source (EBD290002, EXALOS AG) with a central wavelength of 845 nm and a −3 dB bandwidth of 131 nm.[34] The OCM laser was first collimated by a reflective collimator (RC04APC-P01, Thorlabs). A 70:30 (R:T) beam splitter (BS065, Thorlabs) then divided the collimated beam to the sample arm and the reference arm, respectively. The sample arm beam then passed through a homemade conjugated scanning stage, an objective (CFI Plan Fluor 10×, Nikon), and was eventually focused on the sample. As shown in Figs. 2(b) and 2(c), the conjugated scanning stage consisted of a pair of spherical mirrors (10DC100ER.2, Newport) and a pair of galvanometer scanners (CTI6220H, Cambridge Technology). Lateral raster scanning was performed by driving the galvanometer scanners. In the reference arm, the beam also passed through an objective, which is the same as the one in the sample arm, to compensate for dispersion. The back-scattered light from the two arms combined and interfered at the beam splitter. A homemade spectrometer then measured the interferogram. The spectrometer was composed of a diffraction grating, a lens system, and a line camera.[24,34] OCM data acquisition was performed by a frame grabber (PCIe-1433, National Instruments). After data acquisition, standard OCM signal processing (background subtraction, resampling, and fast Fourier transform) was used to reconstruct the depth profile.[35]

For the PAM subsystem, a 532 nm pulsed laser (SPOT-10-100-532, Elforlight) was used as the excitation source. The fiber optic sensor was positioned above the sample to detect the photoacoustic waves. The output of an interrogation laser (TUNICS-T100S-HP, Yenista Optics) was coupled into the sensor fiber. The light reflected from the sensor was directed via a fiber circulator (6015-3-APC, Thorlabs) to a transimpedance amplifier with separate AC and DC coupled outputs. To record the photoacoustic signal, the AC output was connected to a fast digitizer (ATS660, Alazar Technologies, Inc.). To measure the transfer function of the sensor, which is required to determine its optimum bias wavelength, the

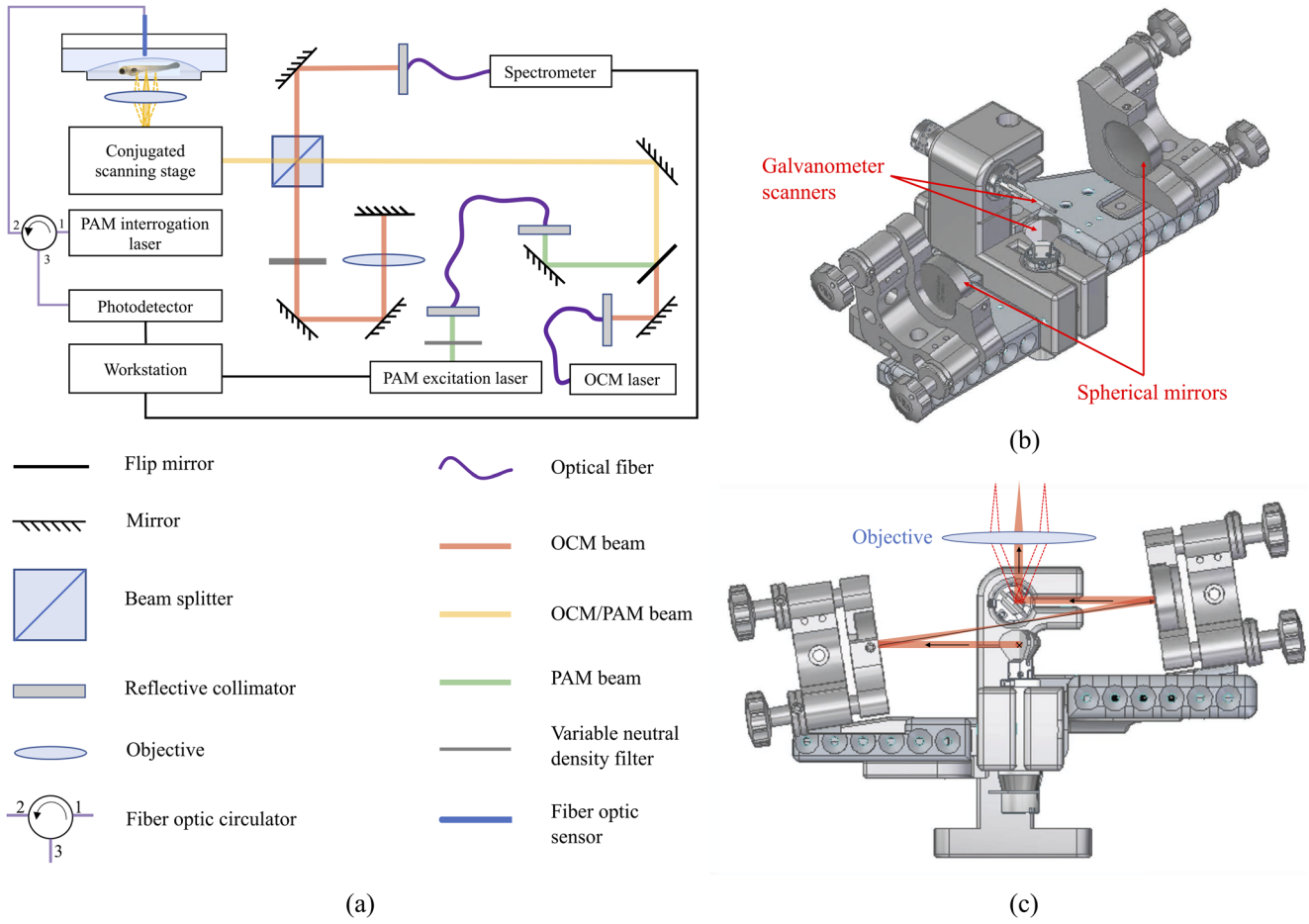

FIG. 2. OC-PAM system: (a) The schematic of the OC-PAM system. (b) The conjugated scanning stage. (c) The front view of the conjugated scanning stage and the beam path.

TABLE I. The OC-PAM system specifications.

	OCM	PAM
Laser wavelength	λ_c[a]: 845 nm $\Delta\lambda$[b]: 131 nm	532 nm
Laser power[c]	1.53 mW	Up to 5.7 mW[d]
Lateral resolution	3.4 μm	1.9 μm
Axial resolution (in air)	3.7 μm	37.3 μm
Sensitivity	104 dB[e]	42.2 Pa[f]

[a]Central wavelength.
[b]−3 dB wavelength bandwidth.
[c]After the objective in the sample arm.
[d]Measured with a 20 kHz pulse repetition rate.
[e]Signal-to-noise ratio measured with a 64 kHz camera line scan rate.
[f]Noise-equivalent pressure over a 20 MHz bandwidth (estimated at 6 MHz given a non-uniform frequency response of the sensor).

DC output was connected to a multifunction I/O card (PCI-6229, National Instruments). The synchronization of the galvanometer mirror, laser triggering, and data acquisition was accomplished by a field-programmable gate array (PCIe-7830, National Instruments).

C. Characterization of the OC-PAM system

The specifications of the OC-PAM system are summarized in Table I.

The lateral resolution for both modalities was measured by imaging a sharp edge on a 1951 USAF resolution target (57-896, Edmund Optics). For the OCM subsystem, the sharp edge was scanned with a step size of 0.21 μm in the x-direction. The maximum intensity projection (MIP) image is shown in the inset of Fig. 3(a). The B-scan along the red dash line was averaged. Then, a smoothing spline function (MATLAB R2018b and Curve Fitting Toolbox 3.5.8, The MathWorks, Inc.) was used to fit the profile to get the edge spread function (ESF). By calculating the first derivative of the ESF and applying a Gaussian curve fitting, the line spread function (LSF) was then obtained. The lateral resolution is defined as the full width at half maximum (FWHM) of the Gaussian fitting curve. The measured lateral resolution for the OCM subsystem was 3.4 μm [Fig. 3(a)]. For the PAM subsystem, the resolution target was imaged with a laser pulse energy of 20 nJ at the sample and at a pulse repetition rate of 20 kHz. The sharp edge was also imaged with a step size of 0.21 μm in the x-direction. The MIP image was obtained after averaging 50 times [as shown in Fig. 3(c), inset]. The measured lateral resolution was 1.9 μm for the PAM subsystem [Fig. 3(c)].

To measure the axial resolution of the OCM subsystem, we imaged a planar silver mirror (PF10-03-P01, Thorlabs). Zero-padding was applied four times to increase the calculation accuracy. After numerical dispersion compensation and Gaussian curve fitting, the axial resolution of the OCM subsystem was defined as the FWHM of the mirror profile along the depth. The measured OCM axial resolution was 3.7 μm [Fig. 3(b)]. To measure the axial resolution of the PAM subsystem, a photoacoustic impulse was obtained by exciting an ultrathin gold film (AU.0100.ALSI, Platypus Technologies, LLC) at the optical focal point. The PAM axial resolution was defined as the FWHM of the envelope of the photoacoustic impulse, which was extracted using the Hilbert transform. The FWHM of the first envelope peak shown in Fig. 3(d) was around 24.9 ns, corresponding to an axial resolution of 37.3 μm for the

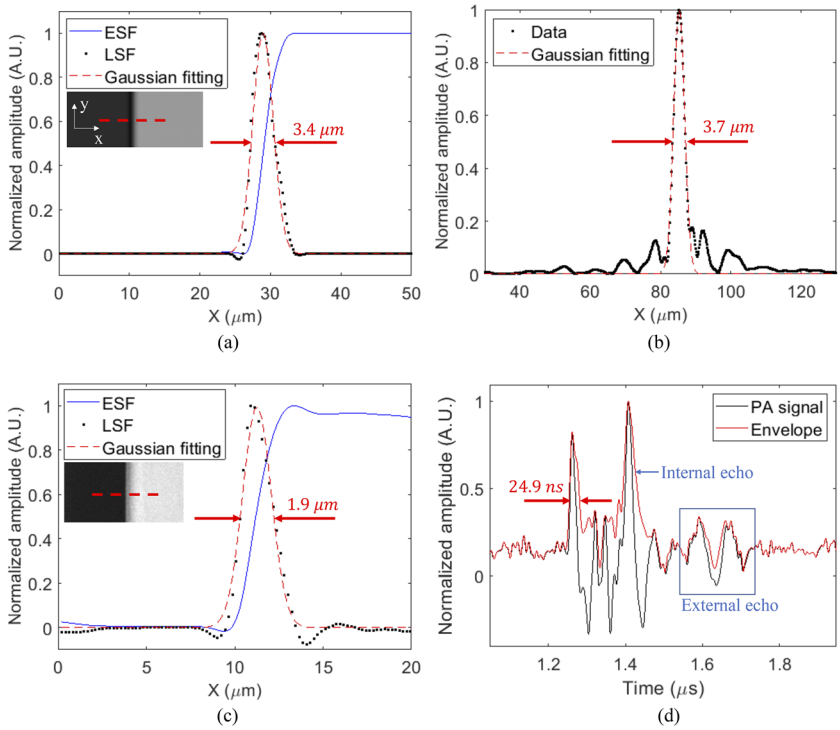

FIG. 3. Characterization of the OC-PAM system: (a) The lateral resolution of the OCM subsystem (inset: the MIP image of the sharp edge). (b) The axial resolution of the OCM subsystem. (c) The lateral resolution of the PAM subsystem (inset: the MIP image of the sharp edge). (d) The axial resolution of the PAM subsystem. ESF: edge spread function; LSF: line spread function.

PAM subsystem. Internal echo from the fiber sensor and external echo from the glass substrate are also included in Fig. 3(d). Without zero-padding and with a 64 kHz camera line scan rate, the measured OCM signal-to-noise ratio was 104 dB. The NEP of PAM at 6 MHz was estimated to be 42.2 Pa over a 20 MHz bandwidth, as described in Sec. II A.

D. Animal preparation

Zebrafish larvae were used in this work to demonstrate the performance of the OC-PAM system. The mitfa$^{b692/b692}$, ednrba$^{b140/b140}$ mutant zebrafish line with reduced melanophores and iridophores was used for spawning. Fertilized eggs were raised in E3 medium at 28 °C. When the zebrafish larvae reached four to five days after fertilization (dpf), we anesthetized them with 0.32 mg/ml tricaine (A5040, Sigma-Aldrich) for 5 min. Then, they were embedded in 1.5% low-melting agarose (9012-36-6, Sigma-Aldrich). Under a brightfield microscope (magnification: 40×, L1000A, GX Microscopes), the zebrafish larvae were gently positioned (sagittal view) in a glass-bottom Petri dish (D35-14-1.5-N, Cellvis). The Petri dish with zebrafish larvae was then mounted on a three-axis translational stage and positioned above the objective in the sample arm [as shown in Fig. 2(a)].

E. *In vivo* zebrafish larva imaging

We imaged three segments (head, trunk, and tail) of three zebrafish larvae individually. Due to the wavelength variation, the foci of the OCM and PAM lasers were different. Therefore, the sample height was adjusted for each modality. OCM *en face* images were generated by average intensity projection using Fiji.[36] The 3D rendering of the OCM image was generated using the 3D Viewer in Fiji.[37] For PAM, the depth ranges were carefully gated to calculate the MIP images. Additional postprocessing of the PAM images included block-matching and 3D filtering,[38,39] contrast limited adaptive histogram equalization,[40,41] and non-local means denoising (OpenCV).[42]

Figure 4 shows the head segment (1.34 × 0.67 mm^2) of zebrafish 1. Since the zebrafish eye has high absorption due to the remaining melanin, this region was avoided during imaging. Figure 4(a) shows the brightfield microscopy image of the FOV. For OCM, the camera line scan rate of the spectrometer was set to 10 kHz, and the acquisition time was around 30 s. For PAM, the excitation laser energy was around 250 nJ after the objective with a pulse repetition rate of 20 kHz. The total acquisition time was around 16 min for 40 times of averaging. The scanning step size was 1.68 μm for both modalities. Figure 4(b) depicts the OCM *en face* image, which showed a good correlation with the brightfield microscopy image and had higher contrast for transparent structures. Although the anatomic details were clearly resolved, the OCM images lacked blood vessel information. On the contrary, the blood distribution was clearly displayed in the PAM image [Fig. 4(c)]. The hepatic vasculature [3 in Fig. 4(c)] and heart chambers [2 in Fig. 4(c)] were also discernible with a high resolution. Figure 4(d) displays the overlaid OCM and PAM images. The OCM image is shown in gray, while the PAM image is depicted in red. Since the two modalities shared the same sample arm, the two images were inherently co-registered in the lateral directions.

The trunk area [0.5 × 0.5 mm^2, Fig. 5(a)] of zebrafish 2 was imaged with a step size of 1.68 μm. The OCM subsystem was set as before. The PAM excitation laser energy after the objective was around 140 nJ with a 20 kHz pulse repetition rate. The image was averaged 40 times, and the total acquisition time was around

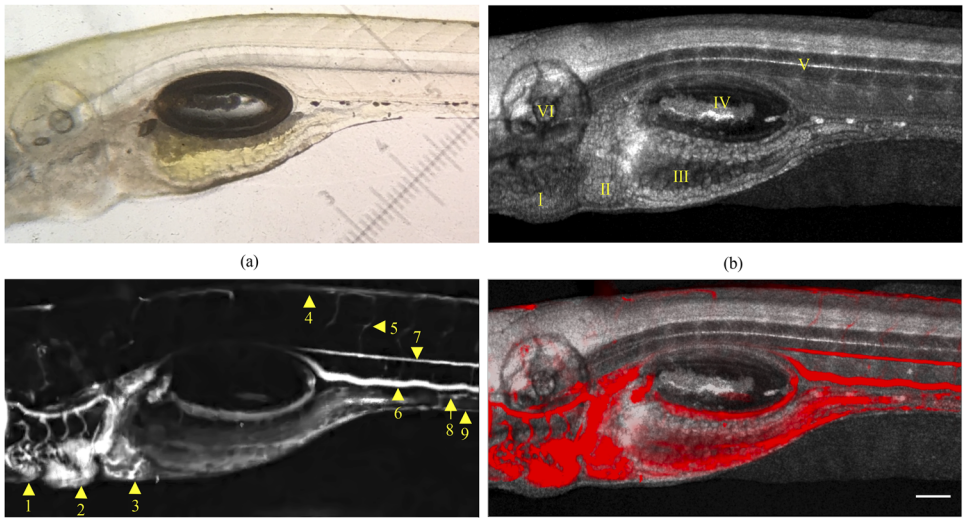

FIG. 4. Head segment (eye excluded) of zebrafish 1: (a) The brightfield microscopy image. (b) The OCM image. (c) The PAM image (logarithm scale). (d) The overlay of (b) and (c) (gray: OCM; red: PAM). I: heart; II: liver; III: yolk and intestine; IV: swim bladder; V: notochord; VI: otic vesicle; 1: aortic arches (AA); 2: heart; 3: liver; 4: dorsal longitudinal anastomotic vessel (DLAV); 5: intersegmental (Se) vessel; 6: posterior cardinal vein (PCV); 7: dorsal aorta (DA); 8: supraintestinal artery (SIA); 9: subintestinal vein (SIV). Scale bar: 100 μm.

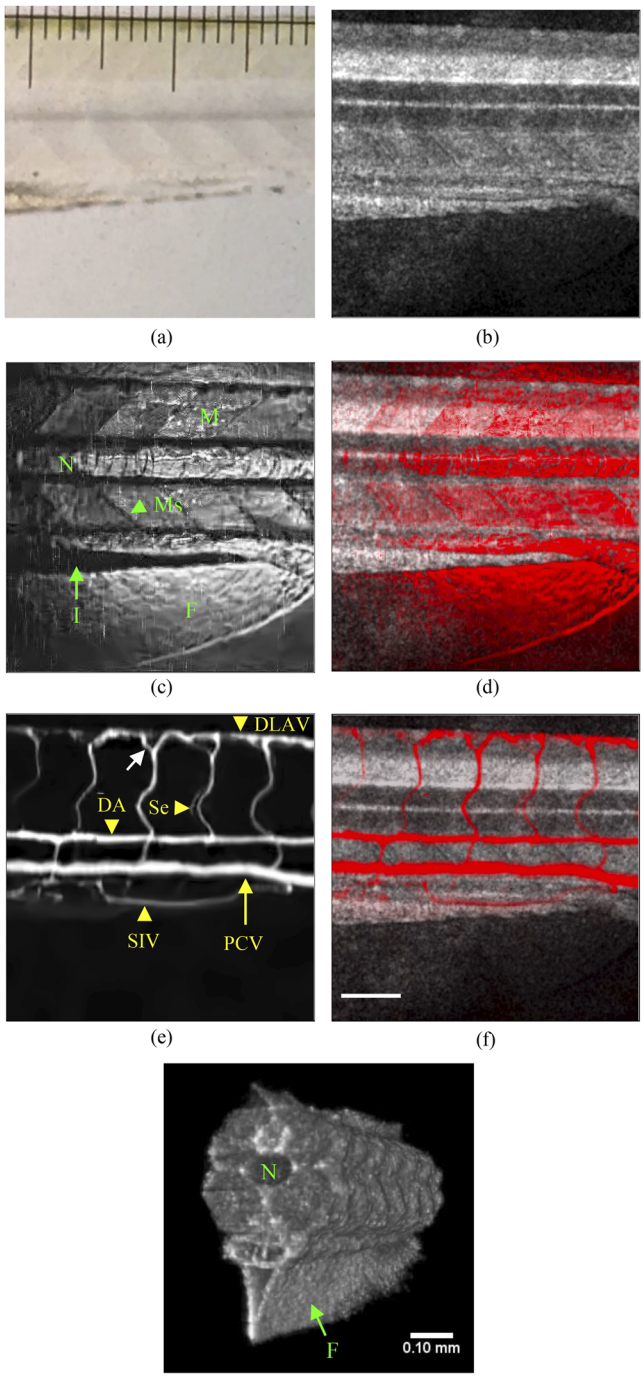

FIG. 5. Trunk segment of zebrafish 2: (a) The brightfield microscopy image. (b) The OCM image. (c) The PAM morphological image (logarithmic scale). (d) The overlay of (b) and (c) (gray: OCM; red: PAM). (e) The PAM vascular image (logarithmic scale). (f) The overlay of (b) and (e) (gray: OCM; red: PAM). (g) 3D rendering of the OCM image. M: myotome; Ms: myosepta; N: notochord; I: intestine; F: fin; DLAV: dorsal longitudinal anastomotic vessel; Se: intersegmental vessel; DA: dorsal aorta; PCV: posterior cardinal vein; SIV: subintestinal vein. Scale bar in (f): 100 μm. Multimedia view: https://doi.org/10.1063/5.0059351.1

5 min. Figure 5(b) shows the OCM *en face* image, and Figs. 5(c) and 5(e) display the morphological and vascular PAM images of the zebrafish, respectively. For the PAM imaging, the morphological and vascular signals were obtained in one volume scan and were separated by the time delay. As shown in Fig. 5(c), the chevron-shaped myotomes separated by the myosepta,[43] fin, and notochord of the zebrafish were distinguishable, whereas the intestine generated nearly no photoacoustic signal. In Fig. 5(e), for one of the intersegmental (Se) vessels [Se arrow in Fig. 5(e)], both segmental artery (SeA) and segmental vein (SeV) were visible. The bifurcation structure [white arrow in Fig. 5(e)] of the dorsal longitudinal anastomotic vessel (DLAV) was also distinct. Figures 5(d) and 5(f) show the overlaid OCM and PAM images. Figure 5(g) shows a static image of 3D rendering of the OCM image, in which the fin is more distinguishable than in Fig. 5(b).

Figure 6(a) exhibits the PAM *en face* image of both morphology and vasculature in the trunk region. Figures 6(b) and 6(c) correspond to the depth profiles at the red star and the green star in Fig. 6(a), respectively. As shown in Fig. 6(b), the photoacoustic signal (PA2) related to the blood absorption was detected at around 1.5 μs, and a high-amplitude echo reached the sensor at about 2 μs. Apart from the blood-generated photoacoustic signal, another photoacoustic signal (PA1) was observed at around 0.1 μs. In the region of the zebrafish fin, no blood-generated photoacoustic signal was detected [as shown in Fig. 6(c)]. However, at around 0.1 μs, a photoacoustic signal (PA3) similar to PA1 was also observed. Therefore, we hypothesize that the PA1 and PA3 aligned with the morphological information on the zebrafish.

At the zebrafish tail, a region [Fig. 7(a)] of 1.37 × 0.5 mm^2 was imaged with a step size of 1.68 μm and 35 times averaging for PAM. The PAM excitation laser energy after the objective was around 270 nJ. Figures 7(b) and 7(c) depict the OCM image and PAM image, respectively. In the PAM image, the caudal artery (CA), the caudal vein (CV), the DLAV, and some of the Se vessels were clearly recognized. Between the CA and CV, we can also see the caudal vein plexus. As some of the Se vessels were not visible in Fig. 7(c), a smaller region [green dash box in Fig. 7(c)] of 0.5 × 0.5 mm^2 was imaged with different sample heights. Then, focus stacking (Adobe Photoshop CC, Adobe, Inc.) was used to generate the inset image of Fig. 7(c). In this focus stacked image, most Se vessels were more distinct, but one of them was still discontinuous. Figure 7(d) displays the overlaid OCM and PAM images.

III. DISCUSSION

This work demonstrates that our OC-PAM system can provide morphological information from the OCM subsystem and vascular images from the PAM subsystem using the fiber optic sensor with a static position. Although PAM is usually applied for chromophore imaging based on absorption contrast, this work also shows its potential in visualizing the zebrafish morphology with an all-optical sensor for the first time. Compared with the OCM image [Fig. 5(b)], the PAM morphological image [Fig. 5(c)] is even better at discerning transparent structures, such as the fin. A possible explanation is that some photons from the excitation laser are not completely attenuated by the sample. The fiber optic sensor then absorbs the transmitted photons and generates photoacoustic signals.[44] Consequently, the sensor-generated photoacoustic signal is stronger at the

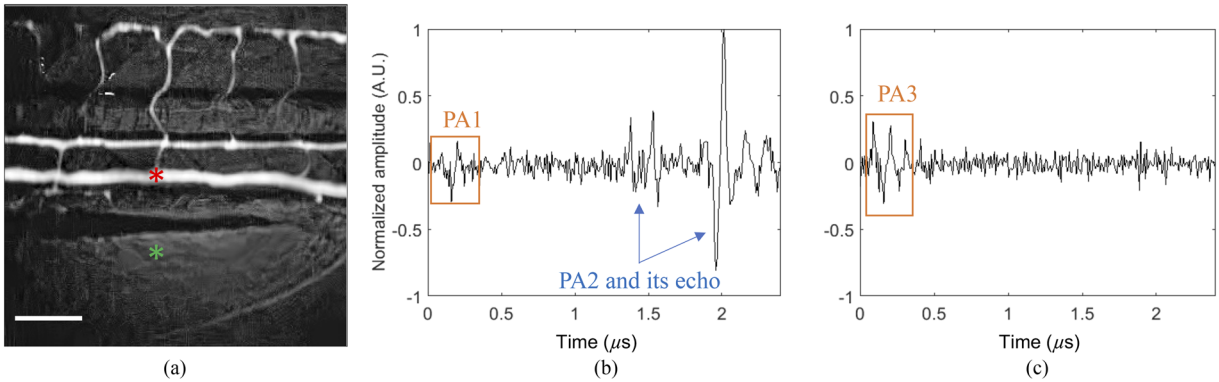

FIG. 6. PAM depth profiles of the zebrafish trunk: (a) The PAM image of both morphology and vasculature (logarithmic scale). (b) The depth profile of position 1 (red star). (c) The depth profile of position 2 (green star). PA1 and PA3: sensor-generated photoacoustic signals; PA2: blood-generated photoacoustic signal. Scale bar: 100 μm.

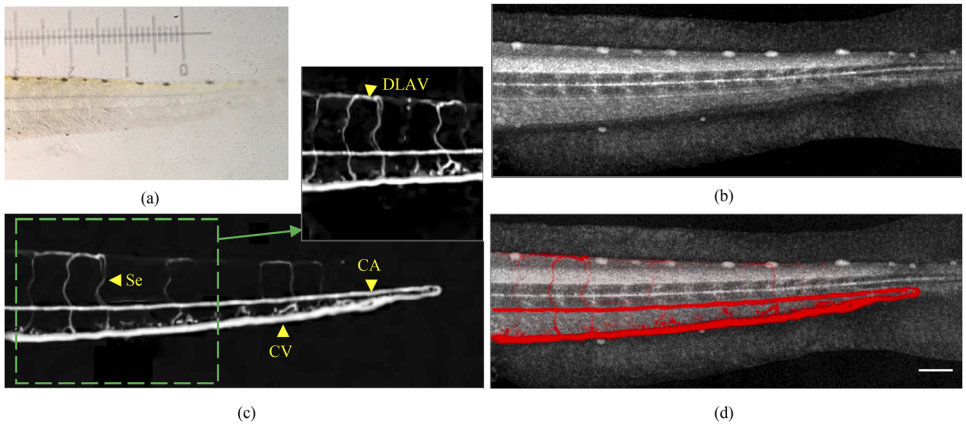

FIG. 7. Tail segment of zebrafish 3: (a) The brightfield microscopy image. (b) The OCM image. (c) The PAM image (logarithmic scale, inset: the focus stacked image of the green dash box region). (d) The overlay of (b) and (c) (gray: OCM; red: PAM). DLAV: dorsal longitudinal anastomotic vessel; Se: intersegmental vessel; CA: caudal artery; CV: caudal vein. Scale bar: 100 μm.

fin [PA3 in Fig. 6(c)] than that at the fish trunk [PA1 in Fig. 6(b)] because the fin is thinner and more transparent. As photons travel faster than phonons, PA1 arrives at the sensor earlier than PA2, as shown in Fig. 6(b). Compared with the OCM images shown in Figs. 4(b) and 7(b), the fin in Fig. 5(b) is less distinct. There are two possible reasons. First, the fin is very thin and transparent compared with the fish body. After average intensity projection and contrast adjustment (the image contrast was adjusted to obtain more information of the fish body), the contrast of the fin is much weakened. Second, as can be seen in the video (multimedia view), the fin was not flat. Since OCM relies on back-scattered photons, the non-flat fin may result in less back-scattered light, which reduces the contrast of the fin, as shown in Fig. 5(b), even further. In comparison, the PAM morphological image depends on transmitted photons. Regardless of the flatness of the fin, the photons can penetrate it and generate photoacoustic signals. In Fig. 5(c), the intestine is darker than other parts. One explanation is that the thick intestine with a granular inner structure absorbs most of the photons, which prevents light penetration. The curved surface of the intestine may also scatter the light away and cause fewer photons to arrive at the sensor. For the head (Fig. 4) and tail (Fig. 7) segments, however, no PAM morphological images were obtained. Several factors may contribute to this result. By comparing the three zebrafish larvae under a brightfield microscope, we found their development and pigmentation varied even though all of them were raised under the same condition. Besides, the position, height, and tilt angle of the fiber optic sensor were not the same for each measurement, which can also affect the detection of penetrated photons. In summary, the imaging results demonstrate that the fiber optic sensor can be used to characterize absorption as well as attenuation features of the sample. Compared with most OC-PAM systems, a single PAM can provide both morphological and vascular information using a simpler, smaller, and cheaper setup. Furthermore, this technique may be applied to quantify the attenuation features of the sample and hence expands the potential applications of PAM in biomedical studies, but additional research is necessary to fully understand the underlying

principles of PAM morphological imaging with the all-optical acoustic sensor.

As shown in Fig. 4(c), the dorsal vessels (4 and 5) were less distinct than the ventral ones (1, 8, and 9). A possible explanation is that the sensor was positioned on the ventral side, so photoacoustic signals from the dorsal side attenuated more when they arrived at the sensor.[45] In the PAM vascular images, some of the Se vessels were not visible or continuous, even when focus stacking was applied. This finding is congruent with literature reports, where some Se vessels of 5 dpf zebrafish were not perfused with enough blood.[46] This finding was verified by imaging the zebrafish with a method called OCT angiography, which is based on motion contrast and not limited to the blood perfusion.[47]

As the PAM subsystem was built in a transmission mode, the OCM beam needed to pass through the glass bottom of the Petri dish, which generates an artifact caused by the glass reflection. To minimize this effect, the Petri dish was tilted during imaging, and a thick layer of agarose was added to the bottom of the Petri dish to increase the distance between the glass bottom and the zebrafish. This procedure had an additional advantage of shifting the otherwise short echo period of the photoacoustic signal (caused by the glass bottom) out of the imaging depth of interest. However, such a procedure also led to a height variance of the zebrafish. Given that only three to four blood cells flow through each Se vessel,[48] the visualization of the Se vessels requires accurate focusing. Therefore, the spatial placement of the zebrafish larvae needs to be adjusted several times to enable more vascular structures to be visualized properly. Although the PAM acquisition time for a large FOV around 1.34×0.67 mm^2 was around 16 min with 40 times of averaging, it takes a long time to refocus when shifting to other imaging regions. As zebrafish larvae need to be sacrificed before 120 h postfertilization according to the ethics requirement, the images in this work were obtained from three different zebrafish larvae. If both high-resolution morphological and vascular images can be obtained from a single PAM system, the OCM subsystem will no longer be needed, and the total image acquisition time can be significantly reduced. Some other factors, such as the fast attenuation of the high-frequency photoacoustic signals and the limited distance and angle for the fiber optic sensor to capture the transmitted photons, also restrict the FOV and require further investigation in the future.

In this work, the OCM subsystem employed a laser with a central wavelength of 840 nm, whereas the PAM subsystem used a 532 nm pulsed laser as the excitation laser. This wavelength mismatch resulted in a focal plane difference and required a sample height adjustment when switching between the two modalities. In the future, a 767 nm pulsed laser will be tested as the PAM excitation laser,[49] which should alleviate this problem and enable simultaneous OC-PAM image acquisition.

Compared with our previous work, in which zebrafish larvae were imaged in an OC-PAM system using an akinetic sensor,[9] the OC-PAM system in this work can visualize the small Se vessels with a higher contrast. As shown in Fig. 1(d), the frequency response of the akinetic sensor peaks at 1 MHz and drops rapidly afterward. This is due to the limited achievable beam width of the interrogation light used for the etalon. For the fiber optic sensor, cavity deformation is measured instead of the refractive index modulation. Thus, the detection bandwidth of the fiber optic sensor is an order of magnitude wider than that of the akinetic sensor. As a result, even though the NEP of the akinetic sensor measured at 1 MHz is much smaller than that of the fiber optic sensor measured at 6 MHz, the fiber optic sensor has an overall higher sensitivity as it has a much broader detection bandwidth, given that the fine structural information is more carried in a higher frequency range.[50] In a few previous reports,[51,52] the volumetric visualization of zebrafish vasculature was achieved by PAM systems using traditional piezoelectric transducers. However, these transducers were centered at a high acoustic frequency with a limited bandwidth, which might ignore photoacoustic signals at lower frequencies. In contrast, the fiber optic sensor covers a wide bandwidth from DC to a high frequency and overcomes this limitation. In addition, due to the wide detection angle of the fiber optic sensor, our OC-PAM is also more flexible with the detector position and can be easily converted to reflection mode imaging. Moreover, in this work, the sensitivity of the fiber optic sensor is limited due to the saturation of the DC channel of the transimpedance amplifier. By implementing an in-fiber attenuator, the sensitivity of the fiber optic sensor can be further improved. Besides, the performance of the fiber optic sensor can also be bettered by optimizing the mirror coatings, investigating other polymers to increase sensitivity, and modifying the tip geometry to improve directivity and bandwidth.[53] In summary, the OC-PAM system using the fiber optic sensor is a valuable tool for the investigation of small animal models such as zebrafish larvae.

IV. CONCLUSION

In this work, it is validated that the fiber optic sensor can be used in a dual-modality OC-PAM system for non-invasive high-resolution *in vivo* imaging. The small size and nearly omnidirectional detection angle of the sensor enable the visualization of a large FOV with a static sensor position. The OC-PAM system reveals not only the scattering and absorption properties but also the attenuation features of the sample. The imaging results clearly illustrate the benefits of such a small and flexible sensor to image small animals, enabling functional imaging and longitudinal studies in the future.

AUTHORS' CONTRIBUTIONS

S.D. and R.H. contributed equally to this work.

ACKNOWLEDGMENTS

This work was supported by the Joint Ph.D. Program Medical University of Vienna/NTU Singapore "Kooperation Singapur" (Grant No. SO10300010), the European Commission Horizon 2020 LEIT Information and Communication Technologies under Grant Agreement No. 732720 (ESOTRAC), the FETOPEN-01-2018-2019-2020-FET-Open Project SWIMMOT under Grant Agreement No. 899612, the H2020-ICT-2020-2 Project REAP under Grant Agreement No. 101016964, the H2020-MSCA-IF-2019 Project SkinOptima under Grant Agreement No. 894325, the European Research Council under Advanced Grant No. 741149, and the Austrian Research Promotion Agency (FFG) under Grant No. 7940628 (Danio4Can).

The authors declare no conflicts of interest.

DATA AVAILABILITY

The data that support the findings of this study are available from the corresponding author upon reasonable request.

REFERENCES

[1] D. Huang, E. A. Swanson, C. P. Lin, J. S. Schuman, W. G. Stinson, W. Chang, M. R. Hee, T. Flotte, K. Gregory, C. A. Puliafito, and J. G. Fujimoto, "Optical coherence tomography," Science **254**(5035), 1178–1181 (1991).

[2] A. F. Fercher, C. K. Hitzenberger, W. Drexler, G. Kamp, and H. Sattmann, "In vivo optical coherence tomography," Am. J. Ophthalmol. **116**(1), 113–114 (1993).

[3] D. Das, A. Sharma, P. Rajendran, and M. Pramanik, "Another decade of photoacoustic imaging," Phys. Med. Biol. **66**, 05TR01 (2021).

[4] P. Beard, "Biomedical photoacoustic imaging," Interface Focus **1**(4), 602–631 (2011).

[5] P. K. Upputuri and M. Pramanik, "Recent advances toward preclinical and clinical translation of photoacoustic tomography: A review," J. Biomed. Opt. **22**(4), 041006 (2017).

[6] W. Drexler, M. Liu, A. Kumar, T. Kamali, A. Unterhuber, and R. A. Leitgeb, "Optical coherence tomography today: Speed, contrast, and multimodality," J. Biomed. Opt. **19**(7), 071412 (2014).

[7] R. A. Leitgeb and B. Baumann, "Multimodal optical medical imaging concepts based on optical coherence tomography," Front. Phys. **6**, 00114 (2018).

[8] S. Jeon, J. Kim, D. Lee, J. W. Baik, and C. Kim, "Review on practical photoacoustic microscopy," Photoacoustics **15**, 100141 (2019).

[9] R. Haindl, A. J. Deloria, C. Sturtzel, H. Sattmann, W. Rohringer, B. Fischer, M. Andreana, A. Unterhuber, T. Schwerte, M. Distel, W. Drexler, R. Leitgeb, and M. Liu, "Functional optical coherence tomography and photoacoustic microscopy imaging for zebrafish larvae," Biomed. Opt. Express **11**(4), 2137–2151 (2020).

[10] X. Zhu, Z. Huang, Z. Li, W. Li, X. Liu, Z. Chen, J. Tian, and C. Li, "Resolution-matched reflection mode photoacoustic microscopy and optical coherence tomography dual modality system," Photoacoustics **19**, 100188 (2020).

[11] X. Liu, T. Liu, R. Wen, Y. Li, C. A. Puliafito, H. F. Zhang, and S. Jiao, "Optical coherence photoacoustic microscopy for *in vivo* multimodal retinal imaging," Opt. Lett. **40**(7), 1370–1373 (2015).

[12] Y. Chang, Y. Hu, Z. Chen, and D. Xing, "Co-impulse multispectral photoacoustic microscopy and optical coherence tomography system using a single supercontinuum laser," Opt. Lett. **44**(18), 4459–4462 (2019).

[13] A. Dadkhah and S. Jiao, "Optical coherence tomography-guided dynamic focusing for combined optical and mechanical scanning multimodal photoacoustic microscopy," J. Biomed. Opt. **24**(12), 121906 (2019).

[14] S. Jiao, Z. Xie, H. F. Zhang, and C. A. Puliafito, "Simultaneous multimodal imaging with integrated photoacoustic microscopy and optical coherence tomography," Opt. Lett. **34**(19), 2961–2963 (2009).

[15] V. P. Nguyen, Y. Li, W. Zhang, X. Wang, and Y. M. Paulus, "High-resolution multimodal photoacoustic microscopy and optical coherence tomography image-guided laser induced branch retinal vein occlusion in living rabbits," Sci. Rep. **9**(1), 10560 (2019).

[16] B. Hermann, M. Liu, N. Schmitner, B. Maurer, D. Meyer, W. J. Weninger, and W. Drexler, "Hybrid ultrahigh resolution optical coherence/photoacoustic microscopy," Proc. SPIE **9323**, 93232N (2015).

[17] M. Liu, "A study of spectral domain optical coherence tomography and photoacoustic microscopy for biometric and biomedical applications," M.S. thesis, Department of Electrical and Computer Engineering, University of Delaware, Newark, DE, 2011.

[18] P. Hajireza, W. Shi, K. Bell, R. J. Paproski, and R. J. Zemp, "Non-interferometric photoacoustic remote sensing microscopy," Light: Sci. Appl. **6**(6), e16278 (2017).

[19] M. T. Martell, N. J. M. Haven, and R. J. Zemp, "Multimodal imaging with spectral-domain optical coherence tomography and photoacoustic remote sensing microscopy," Opt. Lett. **45**(17), 4859–4862 (2020).

[20] P. H. Reza, K. Bell, W. Shi, J. Shapiro, and R. J. Zemp, "Deep non-contact photoacoustic initial pressure imaging," Optica **5**(7), 814–820 (2018).

[21] Z. Chen, S. Yang, Y. Wang, and D. Xing, "All-optically integrated photoacoustic microscopy and optical coherence tomography based on a single Michelson detector," Opt. Lett. **40**(12), 2838–2841 (2015).

[22] C. Blatter, B. Grajciar, P. Zou, W. Wieser, A.-J. Verhoef, R. Huber, and R. A. Leitgeb, "Intrasweep phase-sensitive optical coherence tomography for noncontact optical photoacoustic imaging," Opt. Lett. **37**(21), 4368–4370 (2012).

[23] W. Rohringer, S. Preißer, M. Liu, S. Zotter, Z. Chen, B. Hermann, H. Sattmann, B. Fischer, and W. Drexler, "All-optical highly sensitive broadband ultrasound sensor without any deformable parts for photoacoustic imaging," Proc. SPIE **9708**, 970815 (2016).

[24] R. Haindl, S. Preisser, M. Andreana, W. Rohringer, C. Sturtzel, M. Distel, Z. Chen, E. Rank, B. Fischer, W. Drexler, and M. Liu, "Dual modality reflection mode optical coherence and photoacoustic microscopy using an akinetic sensor," Opt. Lett. **42**(21), 4319–4322 (2017).

[25] J. A. Guggenheim, J. Li, T. J. Allen, R. J. Colchester, S. Noimark, O. Ogunlade, I. P. Parkin, I. Papakonstantinou, A. E. Desjardins, E. Z. Zhang, and P. C. Beard, "Ultrasensitive plano-concave optical microresonators for ultrasound sensing," Nat. Photonics **11**(11), 714–719 (2017).

[26] T. J. Allen, O. Ogunlade, E. Zhang, and P. C. Beard, "Large area laser scanning optical resolution photoacoustic microscopy using a fibre optic sensor," Biomed. Opt. Express **9**(2), 650–660 (2018).

[27] T. J. Allen, J. Spurrell, M. O. Berendt, O. Ogunlade, S. U. Alam, E. Z. Zhang, D. J. Richardson, and P. C. Beard, "Ultrafast laser-scanning optical resolution photoacoustic microscopy at up to 2 million A-lines per second," J. Biomed. Opt. **23**(12), 126502 (2018).

[28] A. Schuermann, C. S. M. Helker, and W. Herzog, "Angiogenesis in zebrafish," Semin. Cell Dev. Biol. **31**, 106–114 (2014).

[29] S. Isogai, M. Horiguchi, and B. M. Weinstein, "The vascular anatomy of the developing zebrafish: An atlas of embryonic and early larval development," Dev. Biol. **230**(2), 278–301 (2001).

[30] G. Kari, U. Rodeck, and A. P. Dicker, "Zebrafish: An emerging model system for human disease and drug discovery," Clin. Pharmacol. Ther. **82**(1), 70–80 (2007).

[31] B. Pelster and W. W. Burggren, "Disruption of hemoglobin oxygen transport does not impact oxygen-dependent physiological processes in developing embryos of zebra fish (*Danio rerio*)," Circ. Res. **79**(2), 358–362 (1996).

[32] E. M. Strohm, E. S. L. Berndl, and M. C. Kolios, "High frequency label-free photoacoustic microscopy of single cells," Photoacoustics **1**(3), 49–53 (2013).

[33] P. C. Beard, A. M. Hurrell, and T. N. Mills, "Characterization of a polymer film optical fiber hydrophone for use in the range 1 to 20 MHz: A comparison with PVDF needle and membrane hydrophones," IEEE Trans. Ultrason., Ferroelectr., Freq. Control **47**, 256–264 (2000).

[34] R. Haindl, M. Duelk, S. Gloor, J. Dahdah, J. Ojeda, C. Sturtzel, S. Deng, A. J. Deloria, Q. Li, M. Liu, M. Distel, W. Drexler, and R. Leitgeb, "Ultra-high-resolution SD-OCM imaging with a compact polarization-aligned 840 nm broadband combined-SLED source," Biomed. Opt. Express **11**(6), 3395 (2020).

[35] R. Haindl, W. Trasischker, B. Baumann, M. Pircher, and C. K. Hitzenberger, "Three-beam Doppler optical coherence tomography using a facet prism telescope and MEMS mirror for improved transversal resolution," J. Mod. Opt. **62**(21), 1781–1788 (2015).

[36] J. Schindelin, I. Arganda-Carreras, E. Frise, V. Kaynig, M. Longair, T. Pietzsch, S. Preibisch, C. Rueden, S. Saalfeld, B. Schmid, J.-Y. Tinevez, D. J. White, V. Hartenstein, K. Eliceiri, P. Tomancak, and A. Cardona, "Fiji: An open-source platform for biological-image analysis," Nat. Methods **9**(7), 676–682 (2012).

[37] B. Schmid, J. Schindelin, A. Cardona, M. Longair, and M. Heisenberg, "A high-level 3D visualization API for Java and ImageJ," BMC Bioinf. **11**, 274 (2010).

[38] Y. Mäkinen, L. Azzari, and A. Foi, "Exact transform-domain noise variance for collaborative filtering of stationary correlated noise," in *IEEE International Conference on Image Processing (ICIP), Taipei, September 2019* (IEEE, 2019), pp. 185–189.

[39] Y. Mäkinen, L. Azzari, and A. Foi, bm3d 3.0.7., available at https://pypi.org/project/bm3d/, June 2020.

[40] J. Ericksen, S. Pizer, and J. Austin, "MAHEM: A multiprocessor engine for fast contrast-limited adaptive histogram equalization," Proc. SPIE **1233**, 322–333 (1990).

[41] Anntzer, clahe 0.1, available at https://pypi.org/project/clahe/, September 2019.

[42]A. Buades, B. Coll, and J.-M. Morel, Non-local means denoising. Image processing on line 1, available at https://doi.org/10.5201/ipol.2011.bcm_nlm, September 2011, pp. 208–212.
[43]C. B. Kimmel, W. W. Ballard, S. R. Kimmel, B. Ullmann, and T. F. Schilling, "Stages of embryonic development of the zebrafish," Dev. Dyn. **203**(3), 253–310 (1995).
[44]M. Moore, E. Strohm, and M. Kolios, "Simultaneous photoacoustic and optical attenuation imaging of single cells using photoacoustic microscopy," Proc. SPIE **9708**, 970850 (2016).
[45]X. L. Deán-Ben, D. Razansky, and V. Ntziachristos, "The effects of acoustic attenuation in optoacoustic signals," Phys. Med. Biol. **56**(18), 6129–6148 (2011).
[46]Y. Chen, L. A. Trinh, J. Fingler, and S. E. Fraser, "Phase variance optical coherence microscopy for label-free imaging of the developing vasculature in zebrafish embryos," J. Biomed. Opt. **21**(12), 126022 (2016).
[47]A. Dadkhah and S. Jiao, "Integrating photoacoustic microscopy, optical coherence tomography, OCT angiography, and fluorescence microscopy for multimodal imaging," Exp. Biol. Med. **245**(4), 342–347 (2020).
[48]T. Karpanen and S. Schulte-Merker, "Zebrafish provides a novel model for lymphatic vascular research," in *Methods in Cell Biology*, edited by H. W. Detrich, M. Westerfield, and L. I. Zon (Academic Press, 2011), Vol. 105, Chap. 9, pp. 223–238.
[49]M. Liu, A. J. Deloria, R. Haindl, Q. Li, G. Szakacs, A. Csiszar, S. Schrittwieser, P. Muellner, R. Hainberger, B. Pelaz, E. Polo, P. del Pino, A. Penttinen, M. Guina, T. Niemi, K. Meiburger, F. Molinari, C. Menhard, J. Heidelin, V. Andresen, D. Geuzebroek, and W. Drexler, "REAP: Revealing drug tolerant persister cells in cancer using contrast enhanced optical coherence and photoacoustic tomography," J. Phys.: Photonics **3**(2), 021001 (2021).
[50]M. M. Vernon and M. Lewin, "Fetal and neonatal echocardiography," in *Avery's Diseases of the Newborn*, 9th ed., edited by C. A. Gleason and S. U. Devaskar (W.B. Saunders, Philadelpia, PA, 2012), Chap. 53, pp. 741–750.
[51]S. Ye, R. Yang, J. Xiong, K. K. Shung, Q. Zhou, C. Li, and Q. Ren, "Label-free imaging of zebrafish larvae in vivo by photoacoustic microscopy," Biomed. Opt. Express **3**(2), 360–365 (2012).
[52]M. J. Moore, S. El-Rass, Y. Xiao, Y. Wang, X.-Y. Wen, and M. C. Kolios, "Simultaneous ultra-high frequency photoacoustic microscopy and photoacoustic radiometry of zebrafish larvae *in vivo*," Photoacoustics **12**, 14–21 (2018).
[53]E. Z. Zhang and P. C. Beard, "Characteristics of optimized fibre-optic ultrasound receivers for minimally invasive photoacoustic detection," Proc. SPIE **9323**, 932311 (2015).